Research Article

In Situ Research on the Spatiotemporal Variations in the Temperature and Deformation of Aeolian Sand-Modified Soil Roadbed Constructed in Cold Regions

Gao Li [1,2,3] **Fubiao Zhou** [4] **Zhandong Su** [5,6] **Jingshan Bo,** [1,2,5] **Xiang Chen,** [7] **and Chi Li** [8]

[1] *Key Laboratory of Earthquake Engineering and Engineering Vibration, Institute of Engineering Mechanics, China Earthquake Administration, Harbin 150000, China*
[2] *Key Laboratory of Earthquake Disaster Mitigation, Ministry of Emergency Management, Harbin 150000, China*
[3] *China Non-ferrous Metals Resource Geological Survey, Beijing 100012, China*
[4] *Institute of Karst Geology, Chinese Academy of Geological Sciences, Guilin 541004, China*
[5] *Geological Engineering Department, Institute of Disaster Prevention, Sanhe 065201, China*
[6] *Hebei Key Laboratory of Earthquake Disaster Prevention and Risk Assessment, Sanhe 065201, China*
[7] *School of Civil Engineering, Beijing Jiaotong University, Beijing 100044, China*
[8] *College of Civil Engineering, Inner Mongolia University of Technology, Hohhot 010051, China*

Correspondence should be addressed to Gao Li; 496527941@qq.com and Zhandong Su; szdchris@163.com

Aiming at the cracking phenomenon of an aeolian sand-modified soil roadbed in an actual project near Tongliao city in eastern Inner Mongolia, Northeast China, an in situ test was conducted. Temperature-compensated fiber Bragg grating (FBG) strain sensors and moisture sensors were embedded into the test roadbed to monitor and observe the relationships between the temperature, moisture, and deformation of the roadbed with respect to variations in climate conditions in such a cold region. For the core issues of roadbed soil deformation and impact on the project, two climate conditions, namely, temperature and rainfall, were taken as external factors, while the temperature and moisture of the roadbed soil were taken as internal factors controlling the deformation and failure of the roadbed soil. A correlation analysis of the test roadbed monitoring data showed that the roadbed soil moisture was weakly affected by environmental conditions. The roadbed soil temperature was independent of the rainfall but was significantly related to air temperature variation (the correlation coefficient ranged from 0.6301 to 0.8926). Limited by the boundary conditions of the roadbed, the response of the variation in the roadbed soil temperature to the air temperature variation gradually weakened from the shallow surface to the deeper parts and the lag in the roadbed soil temperature variation relative to the air temperature variation became more evident. A correlation analysis of the monitoring data of the roadbed soil deformation, soil temperature, and soil moisture showed that the roadbed soil moisture had a weak correlation with the roadbed soil temperature. The roadbed soil deformation was independent of the soil moisture but was strongly related to the roadbed soil temperature. Therefore, the strain of the test roadbed could reflect the roadbed deformation as temperature deformation. The temperature deformation of the roadbed superficial soil was significantly greater than that of the deep soil.

1. Introduction

Aeolian sand, also known as desert sand, wind-blown sand, and dune sand, is sand that is formed, carried, and deposited by wind. The total area of desert, Gobi desert, and desertified land in China is 1.533 million km², including the arid regions of Xinjiang, Gansu, Qinghai, Ningxia, and western Inner Mongolia, as well as the semiarid regions of eastern Inner Mongolia, northern Shaanxi, Liaoning, Jilin, and western Heilongjiang. Summers are scorching, winters are cold, and there is minimal rainfall in these locations. The yearly and daily temperature differences are both significant, with the average annual temperature difference ranging from 30 to 40°C [1]. With the gradual implementation of China's Belt

and Road Initiative and improvement in China's domestic transportation infrastructure, more roads and railroads are expected to eventually pass through desertification zones with large temperature differences.

In cold and arid desert areas, gravel supplies for highway and railway construction are limited. The use of aeolian sand, which is abundant, cheap, and easy to collect, is being explored as a road construction material. However, natural aeolian sand has low bearing capacity, low shear strength, poor uniform particle gradation, lack of cohesion, high porosity, high permeability coefficient, noncollapsibility, low plasticity, and low water content, among other properties. Natural aeolian sand must be modified to generate aeolian sand-modified soil before being used in actual high-grade line engineering. Aeolian sand-modified soil, which is also called aeolian sand-ameliorated/sand-treated/sand-improved soil or aeolian sand-stabilized soil, is a type of mixed material with stable properties realized by adding a modifier into natural aeolian sand. Cement was the very first modification used to improve the compressive and shear strengths of aeolian sand soil [2]. Currently, extensive studies have been conducted on the preparation of materials for cement-modified (stabilization) aeolian sand (including fillered sand grading) [3] in terms of the cement content (8%–25%) [4], water-to-cement ratio, and curing time [2, 4, 5]; and comprehensive modification schemes [6], mechanical properties (including the compressive strength [2–5, 7–10], California bearing ratio (CBR) characteristics [7], shear strength [8, 11–13]; tensile strength [3, 10], maximum dry density, and optimal moisture content [5, 7, 8]); performance testing methods (such as a comparison between compaction methods [14]); and road construction technology [15]. These studies have shown that after full curing, the compressive and shear strengths of aeolian sand-modified soil mixed with an appropriate proportion of cement may be considerably enhanced, meeting roadbed engineering criteria. The findings provide scientific support for the engineering applications of aeolian sand-modified soils.

The surface of a high railway roadbed with aeolian sand-modified soil under construction in Ke'erqin District, Inner Mongolia, was found to exhibit transverse cracks at significantly low temperatures. This case has demonstrated the severity of temperature deformation disease in projects where aeolian sand-modified soil roadbed were constructed [16]. A series of physical and mechanical parameters should be considered in the modification of aeolian sand soil roadbeds in cold and arid regions: thermally induced soil deformation, heat convection between air and soil, internal heat conduction in soil, soil internal temperature field and stress field coupling interaction, degree of soil saturation, soil medium, and soil microstructure. Extensive research has been conducted on thermally induced soil deformation. According to the theoretical framework of thermodynamics and based on soil structure, the interaction of medium in soil caused by temperature variation has been considered [17], and a thermo-hydro-mechanical coupling model of soil has been established [18]. Studies on the cooling and shrinkage deformation law of cement-stabilized aeolian sand-modified soil have found significant soil shrinkage in a

negative-temperature environment [19, 20]. Laboratory investigations revealed that the lower the temperature, the lower the specific heat capacity, and the higher the thermal conductivity of cement-modified (stabilized) soil samples. Under appropriate conditions, a mixture of aeolian sand, cement, and clay can help minimize the temperature sensitivity of modified soils [16, 21, 22].

Existing research on the temperature deformation of aeolian sand-modified soil has mostly focused on theoretical analyses and laboratory soil sample testing; however, there has been no in situ testing of aeolian sand-modified roadbed deformation in a natural environment. The physical and mechanical parameters of aeolian sand-modified soil differ from those of real soil due to sample size limitations; a small-sample test cannot reflect the difference in the internal temperature deformation due to the spatial difference in the soil temperature during the internal heat conduction process. To address these issues, a large-scale in situ test roadbed filled with aeolian sand-modification soil was built beside the Tongliao–Xinmin northern railway project in the cold zone for this study. The monitoring sensor arrangement inside the roadbed was innovatively developed, with several types of sensors paired in nearby areas. This study, for the first time, has achieved multiparameter remote and autonomous monitoring of the soil moisture, temperature, and deformation of a large aeolian sand-modified soil road roadbed constructed in a cold climate setting. This article discusses the temporal and spatial variations in the temperature and deformation of the aeolian sand-modified soil roadbed in cold regions based on the measured data. Moreover, it provides a scientific basis for temperature disease control of aeolian sand-modified soil roadbeds in such regions based on field tests.

2. Materials and Methods

2.1. Geographical Location of the Test Site. The test site was located in Ke'erqin, Inner Mongolia, China (Figure 1). The deformation characteristics of the aeolian sand-modified soil roadbed in a cold region with significant temperature variation were studied relying on the Tongliao–Xinmin high-speed railway project under construction.

The test site is located in the Ke'erqin Sandy Land, which is near the Tongliao city in the middle and lower reaches of the Xiliao River in eastern Inner Mongolia. Bounded by the Daxing'an Mountains in the northwest and the northern Hebei–Liaoxi mountains and hills in the south, high in the west, north, and south, low in the east and in the middle, the Ke'erqin Sandy Land forms a topography with a triangular zone that opens to the east, with an elevation range of 120–1500 m [23]. The Ke'erqin Sandy Land used to be the Ke'erqin Prairie with luxuriant aquatic plants given that the Xiliao River and the Xila Mulun River run through the area from west to east. Due to the open reclamation of wasteland in the late Qing Dynasty and a period of land reclamation in the early days of the founding of the People's Republic of China, the sandy soil layer under the Ke'erqin grassland gradually became desertified. Particularly in recent years, an increase in overloaded grazing and human activities,
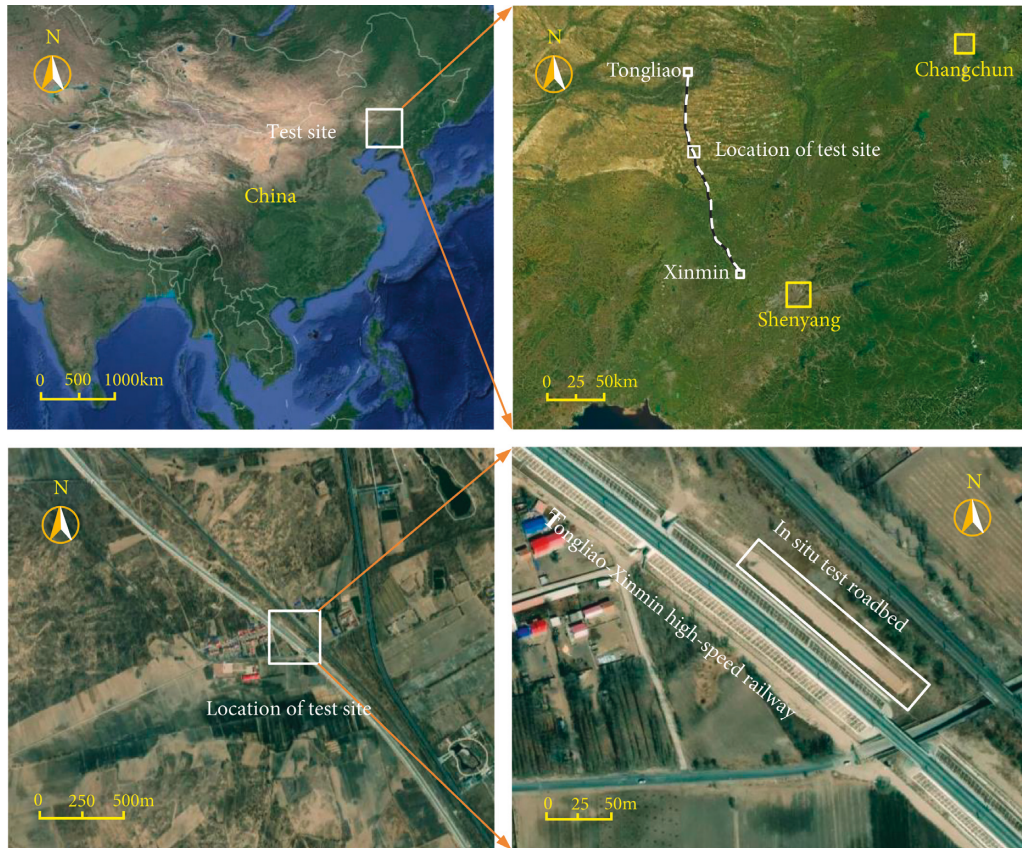
Figure 1: Geographical location of the test site.

coupled with the dry climate, have made parts of this once beautiful grassland to evolve into the largest sandy land in China [24]. The aeolian sand-modified soil made of local natural aeolian sand as the filling material for the Tongliao–Xinmin high-speed railway roadbed is the most economical and reasonable choice for the construction of the Ke'erqin Sandy Railway.

The Tongliao–Xinmin high-speed railway has a total length of 197 km and a design speed of 250 km/h. The railway departs from Tongliao Station and passes through Kezuohou Banner and Zhangwu County, Liaoning Province, and connects to Xinmin North Station of Beijing–Shenyang high-speed railway (Figure 1). Crossing the two provinces of Inner Mongolia and Liaoning, it is the first high-speed railway in Inner Mongolia that is connected to the nationally planned "eight horizontal and eight vertical" high-speed rail network. This is of great significance for Tongliao city to further integrate into the Bohai Sea Rim, Central South Liaoning, and the Northeast Economic Circle, as well as for the integration of Beijing–Tianjin–Hebei and fostering economic development [25].

2.2. Climatic Conditions of the Test Site.
The Ke'erqin Sandy Land, where the test site is located, has a temperate semiarid continental monsoon climate, and temperature variation has resulted in a natural temperature load on the Tongliao–Xinminhigh-speed railway roadbed. Ke'erqin Sandy Land is cold and long in winter, windy and dry in spring, hot and rainy in summer, and cool and short in autumn [24]. The annual precipitation in this area is in the range of 200–650 mm, of which 70% of the precipitation is concentrated during June to August. The annual evaporation is in the range of 1600–2400 mm, mainly concentrated during April to September, which is higher than 78% of the annual evaporation; the multiyear average relative moisture is 55% [26, 27]. Under the influence of the warm low pressure in the Pacific and the cold high pressure in Mongolia, the northwest wind and northerly wind prevail in winter and spring, and the southeast wind prevails in summer. The average annual wind speed is 3.5 m/s, the maximum wind speed is 21.7 m/s, and the number of windy days often reaches approximately 30 days [26, 28]. The annual sunshine hours are above 2800 h, and the annual average frost-free period is 140–150 days [27, 28]. The annual average air temperature is 6.6°C, the extreme maximum air temperature is 36.48°C, and the extreme minimum air temperature is -27.64°C. The temperature difference of the soil at a depth of 1 cm below the ground can reach 30°C or more between day and night. The maximum freezing depth of the sand is 205 cm [29, 30].

2.3. Materials and Parameters.
The aeolian sand utilized in the test roadbed was obtained from the same area of the Tongliao–Xinmin northern railway project. It primarily contained quartz with small quantities of plagioclase and potash feldspar. The maximum dry density was 1.863 g/cm³,

FIGURE 2: Spatial relationship diagram of the test roadbed and the railway under construction.

the specific gravity of the soil particles was 2.685, the nonuniformity coefficient C_u was $2.1 < 5$, and the curvature coefficient C_c was $0.92 < 1$, suggesting that the particles were reasonably uniform and had a poor gradation [21]. The aeolian sand modifier was prepared with regular Portland cement and clay. Portland cement has a strength grade of P.O. 42.5 and an initial setting time of 117 min. Clay has an average moisture content of 8.8%, a plastic index of 10.19, and a liquid index of −0.59. The maximum dry density of the aeolian sand-modified soil mixed with 5% cement and 10% clay was $1.87 \, g/cm^3$, and the best water content was 11.5%, based on laboratory experiments. The unconfined compressive strength and splitting tensile strength of the standard specimen were 0.7479 and 0.0398 MPa, respectively, after seven days of curing [16]. The linear expansion coefficient was $12.15 \, 10^{-6}/°C$ [22].

2.4. Scheme of the Test Roadbed.

The test roadbed was built between and parallel to the Tongliao–Xinmin high-speed railway and the existing railway (Figure 2), with a total length of 150 m. It was divided into five equal roadbed sections constructed with five different modified materials. The bottom width of the roadbed is 15 m, the top width is 7 m, and the height is 4 m. This article discusses the influence of climate on the temperature and deformation of the roadbed of aeolian sand-modified soil based on only the test data of test roadbed Section 1. The mass ratio of the aeolian sand-modified soil material used in the roadbed of test roadbed Section 1 is as follows: cement mixing ratio—5%, clay soil mixing ratio—10%, and aeolian sand mixing ratio—85%.

The test roadbed was located approximately 10 km from the packing mixing station, and the material transit time was less than 20 min. Pumping wells provided water for material mixing and roadbed maintenance near the mixing station and the test section. The mixing station could adjust the moisture content based on the temperature throughout the material mixing operation. The mixing moisture contents were 11.5%, 12.5%, and 13.5% in the temperature ranges of 20–25, 25–30, and 30–35°C, respectively. Eight dump-type transport vehicles ($26.5 \, m^3$/vehicle) were employed to fill the roadbed. To maximize the management of water, the top of the transport vehicle was covered with light-colored geotextiles while transporting the supplies. After the packing was brought to the dumping location, the paving and rolling of the packing were completed promptly, and a bulldozer and a roller were used for continuous paving and rolling. Light-colored geotextiles were covered after rolling to avoid moisture (Figure 2). The duration between the start of material transportation and the completion of roadbed compaction should not exceed 117 min; that is, compaction must be finished prior to the initial setting of cement. Because the transverse cracks were presented before the surface roadbed material and auxiliary facilities setting, the roadbed surface materials of the experimental section and the actual operation roadbed are therefore not the same.

Roadbed filling: the filling and compaction tests were conducted in accordance with the Construction Code for Railway Roadbed (TB 10202–2002) [31]. The paving method combining layered filling, vibration compaction, and static compression is based on the assumption that the compaction degree is not less than 92% and that the seven-day unconfined compressive strength is not less than 0.25 MPa. By layering each layer with a thickness of 35 cm (compaction thickness of 30 cm and a loosening coefficient of 1.16), the optimal moisture content was 11.5%, and there were six

(a)

(b)

(c)

(d)

(e)

(f)

Figure 3: Continued.

(g)

(h)

FIGURE 3: Temperature, humidity, and deformation sensors embedded in the test roadbed soil and data collection terminal. (a) Buried groove excavation, (b) fiber optic cable layout, (c) humidity sensor, (d) burying of humidity sensor, (e) humidity sensor data collection terminal, (f) fiber grating (temperature) strain sensor, (g) embedded fiber grating (temperature) strain sensor, and (h) strain sensor data acquisition terminal.

compaction cycles (static pressure 1 time ⟶ weak vibration 1 time ⟶ strong vibration 2 times ⟶ weak vibration 1 time ⟶ static pressure 1 time). A combination of 22 t and 18 t rollers was used; the first static compaction and vibration compaction were performed by the 22 t roller, and the last static compaction and vibration compaction was performed by the 18 t roller. The longitudinal roller track overlap between the rows was greater than 40 cm, the longitudinal lap length was greater than 2 m, and the staggered joints of the upper and lower layers were greater than 3 m. Huge rollers cannot be employed within a 1 m range of the roadbed slope; therefore, small vibration rammer compaction was used instead. When a layer of filling qualified in the initial setting before the next filling layer is built, no additional care is required. If the next layer of paving is not completed before the initial setting due to sensor embedment or other reasons, the geotextile sprinkler maintenance must be completed within seven days.

2.5. Sensors and Layout. An appropriate number of temperature-compensated FBG strain sensors (mark graphic ▲, code TS, used for both temperature and deformation monitoring), FBG ordinary strain sensors (mark graphic △, code S, used for soil deformation monitoring) [32], and plug-in probe soil moisture sensors (mark graphic ○, code W, used for soil moisture monitoring) were embedded into the test roadbed. This was done to monitor the spatial distributions of the temperature, deformation, and moisture of the test roadbed soil in the cold climate environment, considering the sensor spatial distribution and cost (Figure 3). The sensors were embedded at the same time as roadbed filling. The sensors and wire were embedded in the positioning layer by digging a 0.2 m deep trench after the

filler was filled 0.2 m above each positioning layer (F1–F5). Before the paving of next layer , the trench was backfilled with aeolian sand-modified soil before initial setting and compacted.

All the sensors were embedded at the space monitoring node of the test roadbed formed by the intersection of three vertical planes perpendicular to the long axis of the roadbed (abbreviated as cross sections H1, H2, and H3 from NW to SE), five horizontal planes (abbreviated as horizontal planes F1–F5 from bottom to top), and seven vertical longitudinal planes parallel to the long axis of the roadbed (abbreviated as longitudinal sections L1–L7 from NE to SW) (Figure 4). The long axis of all the deformation sensors embedded into the roadbed soil was consistent with the long axis of the test roadbed, and the deformation of the roadbed soil measured by the sensors was the deformation along the long axis of the roadbed.

Using a combination of letters and Arabic numerals to mark the sensors in the monitoring node in the roadbed, the first letter H corresponds to the cross section, and the numbers 1 to 3 represent cross sections H1–H3, respectively. The second letter F corresponds to the horizontal plane, and the numbers 1–5 represent the horizontal planes F1–F5, respectively. The third letter L corresponds to the longitudinal section, and the numbers 1 to 7 correspond to the longitudinal sections L1 to L7, respectively. For example, node numbers H2-F3-L4 represent nodes where cross section H2, the horizontal plane F3, and the longitudinal section L4 intersect. Furthermore, each sensor in the roadbed is assigned a unique number: node number + sensor type code, for example, the number H1-F2-L3-TS represents the temperature-compensated FBG strain sensor embedded at the monitoring node "H1-F2-L3" (the intersection between cross section H1, horizontal plane F2, and longitudinal section L3).

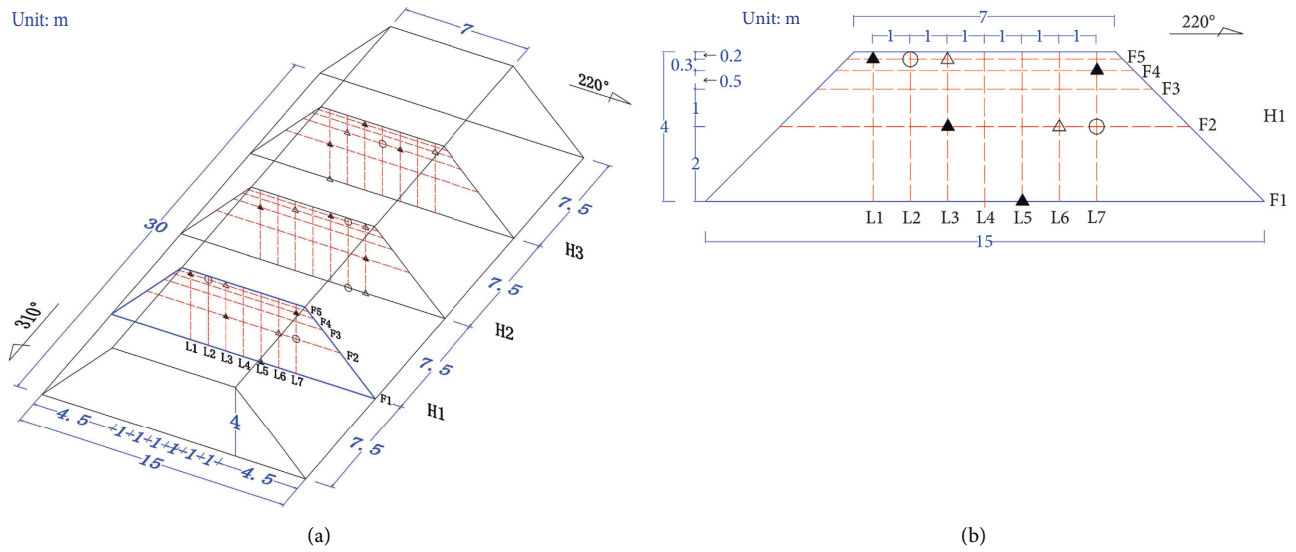(a)   (b)

FIGURE 4: Schematic of the size of a single section of the aeolian sand-modified soil test roadbed and the location of the sensors. (a) Three-dimensional spatially diagram of the embedded sensor nodes and (b) position of the five horizontal planes and seven longitudinal planes.
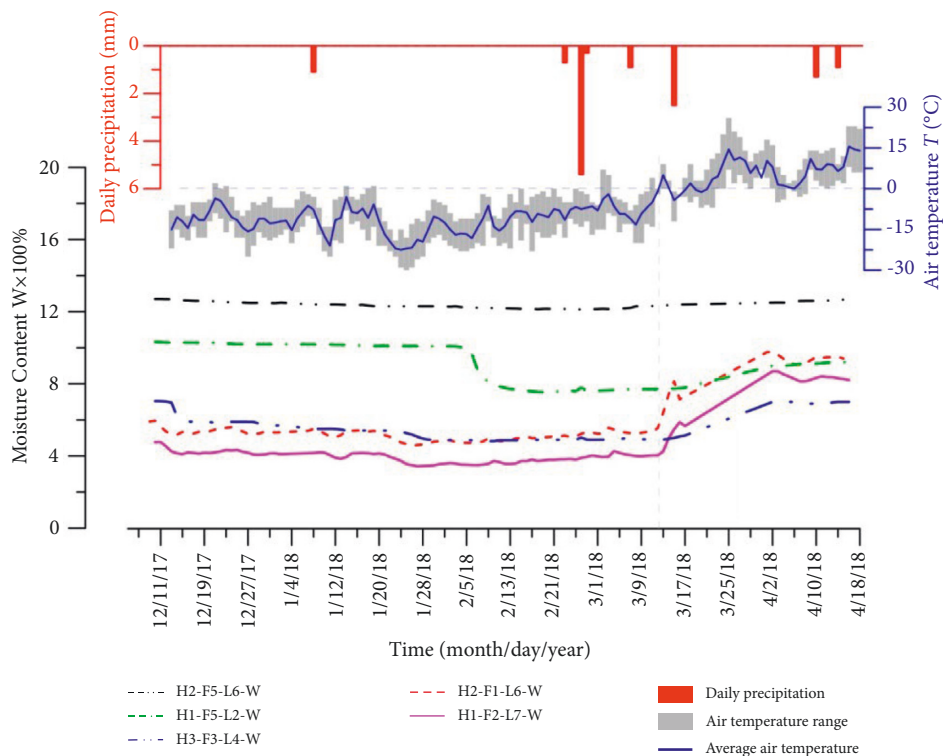

FIGURE 5: Curves of soil moisture of each layer in the roadbed under climatic conditions.

The sensors in the test roadbed were connected to the modem and data acquisition equipment via signal cables, and the moisture, temperature, and strain data were automatically collected and uploaded to the cloud platform through a wireless network. Thus, the monitoring data were collected remotely and uninterruptedly.

3. Monitoring Results

The sensors embedded into the roadbed produced monitoring data for a winter spanning from December 2017 to April 2018. The air temperature and rainfall data of the study area during the same monitoring period were obtained from the website of China National Meteorological Administration.
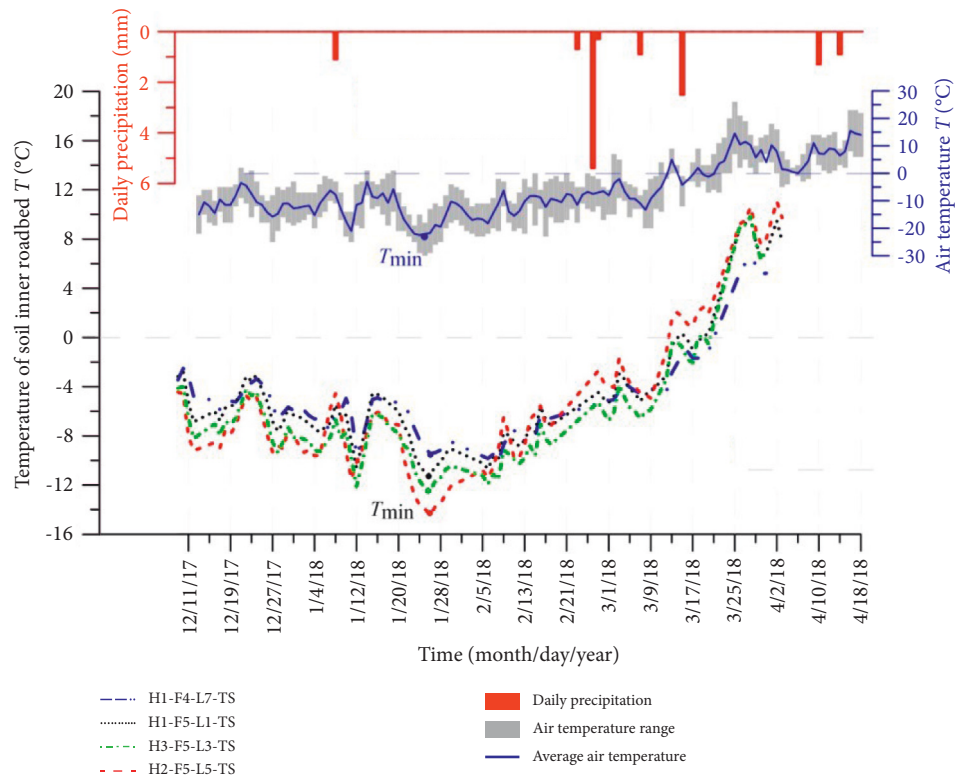
FIGURE 6: Curves of soil temperature in the F5 and F4 layers of the roadbed under climatic conditions.

3.1. Temporal and Spatial Variations in the Soil Moisture under Climatic Conditions. Figure 5 shows that during the monitoring period, the soil moisture in the F5 layer of the roadbed is relatively high, the soil moisture variation at H2-F5-L6-W is in the range of 12.1%–12.7% under the influence of the air temperature and rainfall, and the soil moisture variation curve is relatively straight. However, the curve of the soil moisture at H1-F5-L2-W drops significantly around February 5, 2018. It is speculated that the cause of this phenomenon is the cracking and expansion of the soil, which makes the low-temperature air to enter and the water to freeze, thus resulting the decline in soil moisture. The moisture in the soil layers F1, F2, and F3 is mainly in the range of 4%–6% during the period of negative average air temperature. When the average air temperature rises to positive (−2°C on March 12, 2018, 3°C on March 13, 2018), the soil moisture in the F1, F2, and F3 layers increased, of which F1 and F2 increased significantly, with an increase of approximately 5%, while the increase in the soil moisture of layer F3 is relatively small, with an increase of approximately 2%. The daily precipitation on February 26, 2018 was 5.4 mm; however, the moisture in each layer of the roadbed did not vary significantly due to the rainfall, indicating that the moisture of the roadbed soil is slightly affected by the small rainfall in cold and arid areas.

3.2. Temporal and Spatial Variations in the Soil Temperature under Climatic Conditions. The distances from the top surface of the test roadbed to the F5 and F4 layers are 20 and

50 cm, respectively. Figure 6 shows that the soil temperature curves of the three sensors in the F5 layer are more consistent and have better synchronization with the air temperature variation, while the soil temperature curve of the F4 layer slightly lags behind the air temperature variation, particularly when the air temperature changes from negative to positive. The temperature of the soil near the top of the roadbed responds more instantly and sensitively to variations in the air temperature in general.

The distance from the top surface of the test roadbed to the F2 layer is 200 cm. Figure 7 shows that the soil temperature of the F2 layer in the roadbed remains at negative temperature when the air temperature rises to positive. There is an evident lag effect between the time of the lowest temperature of the roadbed soil and the time of the lowest air temperature.

Figure 8 shows that the closer to the surface of the roadbed, the greater the effect of the air temperature on the soil temperature and the greater the range of soil temperature variation. When the air temperature varies in the range of −22.5–18°C, the sensors H1-F5-L1-TS, H1-F4-L7-TS, and H1-F2-L3-TS record the soil temperature varying in the ranges of −11.2–9.7°C, −10–9.8°C, and −9.3 to −1.3°C, respectively, and the time of the lowest soil temperature lags behind the lowest air temperature by 2, 15, and 38 days, respectively. This shows that the shallower the monitoring node, the more sensitive the soil temperature to the air temperature variation. The specific performance is as follows: in the cooling process, the soil temperature at the shallow node cools faster, and the lowest temperature is
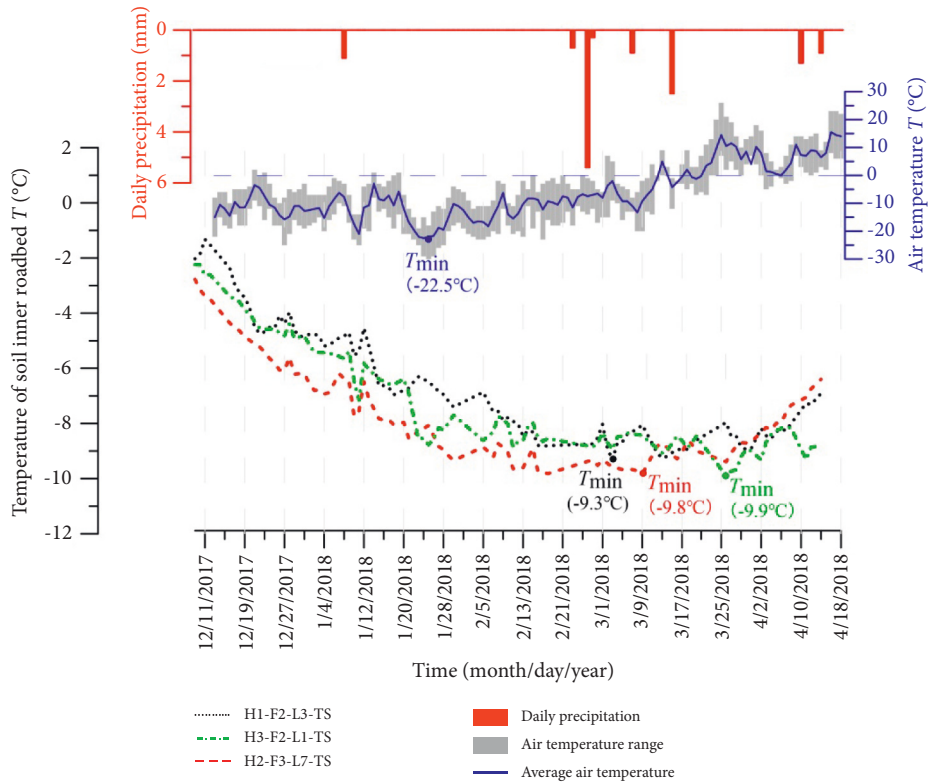
FIGURE 7: Curves of the soil temperature of the F2 layer in the roadbed under climatic conditions.
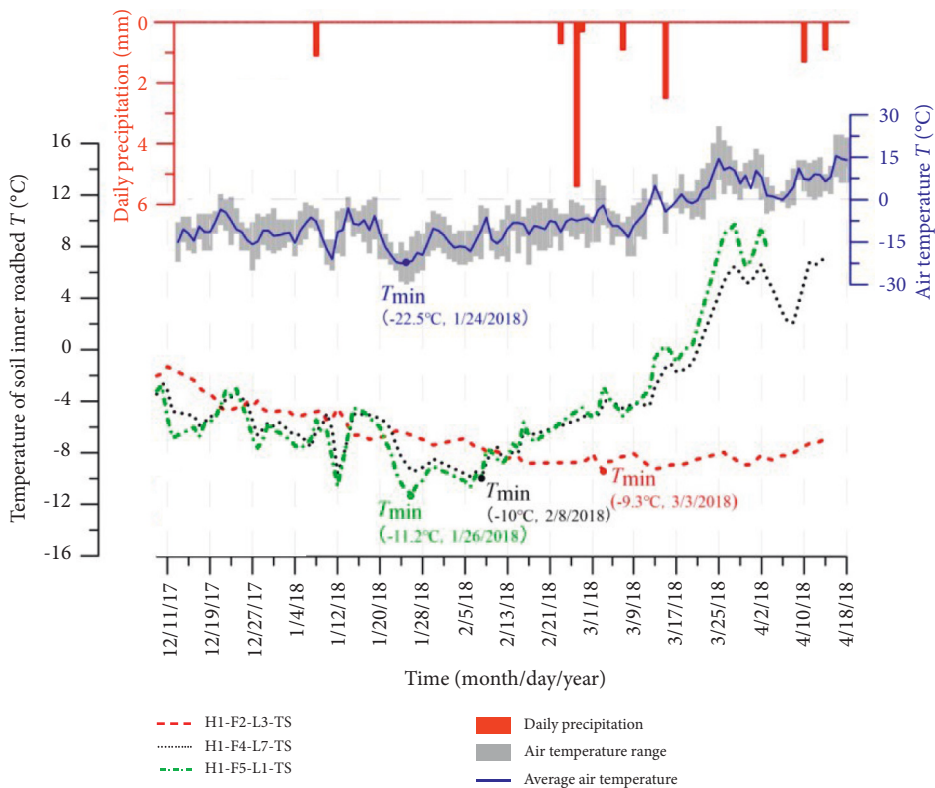

FIGURE 8: Curves of soil temperature in the F5, F4, and F2 layers of the roadbed under climatic conditions.
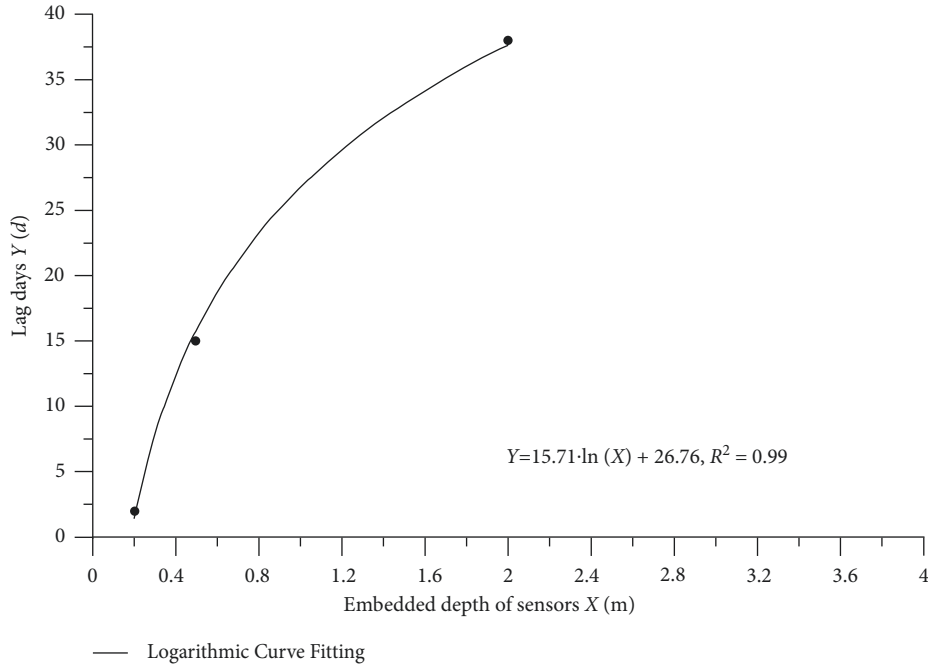
Figure 9: Relationship between the lag days of the minimum soil temperature relative to the minimum air temperature and the embedded depth of the monitoring sensor.

Table 1: Lag days of the minimum soil temperature relative to the minimum air temperature, the embedded depth of the monitoring sensor, and the variation range of the soil temperature.

Sensor number	Lag days (d)	Depth (m)	Minimum soil temperature (°C)	Variation range of the soil temperature (°C)
H1-F5-L1-TS	2	0.2	−11.2	−11.2 to 9.7
H1-F4-L7-TS	15	0.5	−10	−10 to 9.8
H1-F2-L3-TS	38	2.0	−9.3	−9.3 to −1.3

lower than that at the deep node. In the heating process, the soil temperature at the shallow node rises faster, and the highest temperature at that node is relatively higher. Based on Figures 6–8, it can be seen that from the surface to the inside, from shallow to deep, the internal soil temperature of the test roadbed is unevenly distributed and varies with time differently under the cold climatic condition.

A relationship is established (Figure 9) on the basis of the lag days of the minimum soil temperature relative to the minimum air temperature and the embedded depth (the distance between the monitoring node and the top surface of the roadbed) of the monitoring sensors (Table 1).

Figure 9 shows that the farther away from the top surface of the roadbed, the more evident the hysteresis effect of the lowest soil temperature relative to the lowest air temperature. The relationship between the lag days (Y) and the embedded depth of the sensor (X) is logarithmic curve fitted, and the equation of the logarithmic curve is $Y = 15.71 \cdot \ln(X) + 26.76$, $R^2 = 0.99$.

3.3. Temporal and Spatial Variations in the Soil Deformation under Climatic Conditions.
The unit of the small deformation of the modified soil recorded by the strain sensors is microstrain ($\mu\varepsilon$). A positive strain reading indicates that the

strain sensor is under tension, that is, the soil where the sensor is embedded has expanded or stretched. Conversely, a negative strain reading indicates that the strain sensor is compressed, that is, the soil where the sensor is located has shrunk.

The soil strain variation curves in Figure 10 show that the strain of the soil in the F5 layer is much greater than that in the F2 layer. The soil strain variation in the F2 layer is −73.8 to 214.8 $\mu\varepsilon$ during the monitoring period; however, the soil strain variation in the F5 layer is −889.5 to 694.9 $\mu\varepsilon$. The trend in the soil strain variation at the same layer is the same, and the difference in the soil strain at different positions in the same layer is small, but significant in different layers.

Figure 11 shows that the variation trend and magnitude of the soil strain at each layer in the roadbed are different under the same climatic condition. The positive and negative soil strains in the F3, F4, and F5 layers of the roadbed are greater than those in the F1 and F2 layers in general. The absolute value of the soil maximum strain in the F1 and F2 layers does not exceed 300 $\mu\varepsilon$, but those in the F3, F4, and F5 layers are greater than 600 $\mu\varepsilon$. During the period of negative air temperature, the soil strains in the F3, F4, and F5 layers are all negative, and the soil strain amount relationship is F5 > F4 > F3. During the period of positive air temperature, the soil strains in the F3, F4, and F5 layers are positive, and the soil strain amount relationship is the same, F5 > F4 > F3.
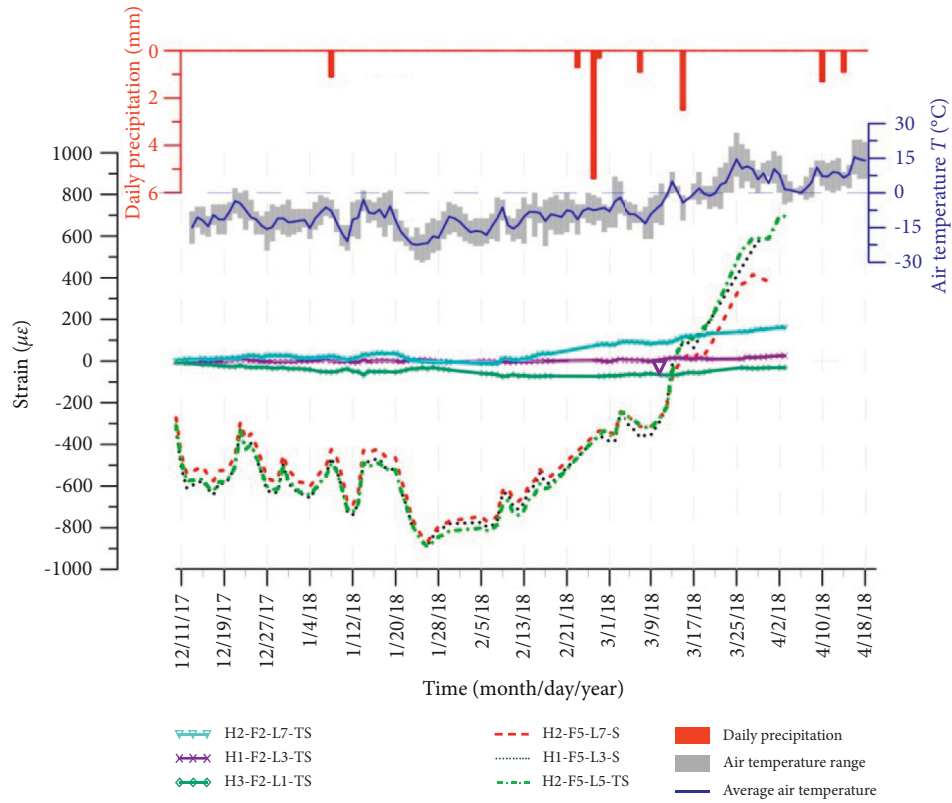
FIGURE 10: Curves of soil deformation in the F5 and F2 layers of the roadbed under climatic conditions.
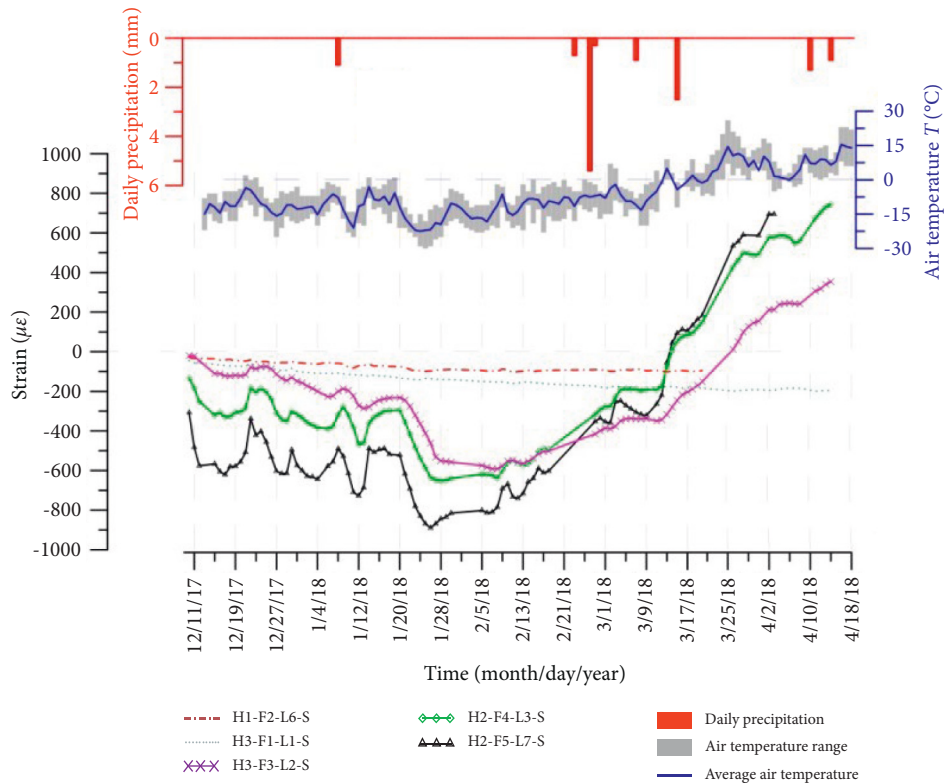

FIGURE 11: Curves of soil deformation of five layers in the roadbed under climatic conditions.

TABLE 2: Relationship between correlation coefficient $|r_{xy}|$ and strength of correlation.

$|r_{xy}|$	0–0.2	0.2–0.4	0.4–0.6	0.6–0.8	0.8–1.0
Strength of correlation	Irrelevant	Weak correlation	Moderate correlation	Strong correlation	Very strong correlation

TABLE 3: Correlation between the variations in the soil temperature and air temperature and rainfall.

Sensor number of soil temperature	Correlation between the variations in soil temperature and air temperature $|r_{xy}|$	Correlation between the variations in soil temperature and rainfall $|r_{xy}|$
H1-F5-L1-TS	0.8059	0.0855
H2-F5-L5-TS	0.8926	0.1232
H3-F5-L3-TS	0.8171	0.1190
H1-F4-L7-TS	0.6301	0.0778

The soil deformation monitoring results show that during negative air temperature, the soil in the F3, F4, and F5 layers exhibited shrunk deformation, and all have tensile deformation during positive air temperature. However, the strain amounts of these three layers are different even when they are under the same air temperature. The closer to the top surface of the roadbed, the greater the negative strain of the soil at the low temperature and the positive strain at high temperature, the greater the amplitude of the strain variation, and the more evident and sensitive the response of the soil strain to the air temperature.

The response of the soil strain at different locations of the test roadbed to the same air temperature has significant temporal and spatial differences, resulting in an uneven distribution of the soil deformation in the roadbed, which is the fundamental reason for cracking in the roadbed soil. According to a previous study, the critical tensile strain for cracking and deformation of the top surface of the roadbed is 600 $\mu\varepsilon$ [33]. Therefore, based on the results of the roadbed strain monitoring data, the following part of the article will focus on the analysis of the factors affecting soil deformation and cracking in roadbed layers F3, F4, and F5.

4. Correlation Analysis of Factors Influencing Roadbed Soil Deformation

The change process of the soil moisture, temperature, and deformation over time in the static roadbed can be attributed to the variation in the external environment conditions, which are the air temperature and rainfall. The variations in the air temperature and rainfall directly cause changes in the temperature and humidity of the roadbed soil. The changes in the temperature of the roadbed soil further lead to changes in the soil deformation and soil moisture, and the impact of the soil moisture change on the soil deformation should be evaluated.

The variations in the soil moisture, temperature, deformation, and air temperature constitute four types of data series. The correlation analysis method is used to explore the effects of the air temperature on the soil temperature, humidity, and strain to determine the main external influencing factors leading to soil deformation and crack formation. The value of the correlation coefficient between the variation in the air temperature and the change in the soil

temperature, and soil humidity is determined, as well as the correlation coefficient between the change in the soil temperature, soil humidity, and soil strain, to judge the strength of the correlation. If the correlation is strong, the impact will be significant, and vice versa, the impact will be small. The correlation analysis method is as follows:

Suppose there are two data series: $X = \{x_i\}$ and $Y = \{y_i\}$, $i = 1, 2, 3, \ldots, n$, and their average values can be expressed as

$$\overline{x} = \frac{1}{n} \sum_{i=1}^{n} x_i$$
$$\overline{y} = \frac{1}{n} \sum_{i=1}^{n} y_i. \tag{1}$$

The correlation coefficient r_{xy} of the two data series is calculated using the following formula:

$$r_{xy} = \frac{\sum_{i=1}^{n} (x_i - \overline{x}) \cdot (y_i - \overline{y})}{\sqrt{\left(\sum_{i=1}^{n} (x_i - \overline{x})^2\right) \cdot \left(\sum_{i=1}^{n} (y_i - \overline{y})^2\right)}}. \tag{2}$$

The value range of the correlation coefficient is $-1 \le r_{xy} \le +1$, where $r_{xy} < 0$ indicates that X is negatively correlated with Y; $r_{xy} > 0$ indicates that X and Y are related; and $r_{xy} = 0$ implies that X and Y are irrelevant [34, 35]. The greater the $|r_{xy}|$ value, the stronger the relationship between X and Y. The correlation coefficient $|r_{xy}|$ and the related degree of the recommended classification comparison relationship was referred from Xiao Yong and Shao Fan [36, 37], as listed in Table 2. The following qualitative description of the correlation strength follows the recommended interpretation of r_{xy}: 0.0–0.2: irrelevant; 0.2–0.4: weak correlation; 0.4–0.6: moderate correlation; 0.6–0.8: strong correlation; and 0.8–1.0: very strong correlation, although other interpretations have been made [38–40].

4.1. Correlation Analysis between Internal Factors of Roadbed Soil Deformation and External Factors. In the crack formation and deformation processes of the soil, the internal factors are direct influencing factors, whereas the external factors indirectly affect the soil deformation by affecting the internal factors. A correlation analysis between the external factors (air temperature and rainfall) and the internal factors

TABLE 4: Correlation between the variation in the soil moisture and the rainfall.

Sensor number of soil moisture	Correlation between the variation in the soil moisture and the rainfall $\lvert r_{xy}\rvert$
H1-F5-L2-W	0.1595
H2-F5-L6-W	0.0117
H3-F3-L4-W	0.0886

TABLE 5: Correlation coefficient of roadbed soil temperature and soil moisture.

Correlation coefficient of soil temperature and soil moisture $\lvert r_{xy}\rvert$	H1-F5-L1-TS	H2-F5-L5-TS	H3-F5-L3-TS	H1-F4-L7-TS
H1-F5-L2-W	0.3230	0.5724	0.3367	0.1754
H2-F5-L6-W	0.2219	0.0390	0.2126	0.3263
H3-F3-L4-W	0.1127	0.1550	0.0829	0.2758

TABLE 6: Correlation coefficient of roadbed soil deformation and soil moisture.

Sensor number of soil moisture	Sensor number of soil deformation	Correlation coefficient between soil deformation and soil moisture $\lvert r_{xy}\rvert$
H1-F5-L2-W	H1-F5-L3-S	0.5064
	H1-F5-L1-TS	0.1458
H2-F5-L6-W	H2-F5-L7-S	0.0875
	H2-F5-L5-TS	0.0650

TABLE 7: Correlation coefficient of roadbed soil deformation and soil temperature.

Sensor number of soil temperature	Sensor number of soil deformation	Correlation coefficient between soil deformation and soil temperature $\lvert r_{xy}\rvert$
H3-F5-L3-TS	H3-F5-L3-TS	0.9332
	H2-F5-L7-S	0.9652
	H2-F5-L5-TS	0.9508
	H1-F5-L3-S	0.9593
H2-F5-L5-TS	H2-F5-L5-TS	0.9744
	H2-F5-L7-S	0.9651
	H2-F5-L5-TS	0.9533
	H1-F5-L3-S	0.9665
H1-F5-L1-TS	H1-F5-L1-TS	0.8227
	H2-F5-L7-S	0.9708
	H2-F5-L5-TS	0.9515
	H1-F5-L3-S	0.9571
H1-F4-L7-TS	H1-F4-L7-TS	0.9598
	H2-F4-L3-S	0.9845
	H3-F4-L7-S	0.9758

(soil temperature and soil moisture) that produce deformation and cracks in the roadbed soil should be conducted.

Table 3 shows that the correlation coefficient between the soil temperature in the F5 layer and the air temperature is greater than 0.8, which represents a very strong correlation; the value of the correlation coefficient between the soil temperature in the F4 layer and the air temperature is between 0.6 and 0.8, representing a strong correlation, while the correlation coefficients between the soil temperature in the F5 and F4 layers and rainfall are less than 0.2, representing an irrelevant result. The correlation analysis results show that the change in the roadbed soil temperature is significantly affected by the variation in the air temperature, irrespective of the rainfall. The variation in the air temperature is the main reason for the change in the soil temperature of the roadbed.

Table 4 shows the correlation analysis results of the change in the soil moisture monitored by the moisture sensors in the F3 and F5 layers and the rainfall recorded in Figure 5. The results show that the correlation coefficients between the roadbed soil moisture and rainfall are less than 0.2, representing an irrelevant result. This shows that the very little rainfall in the cold and arid areas cannot significantly affect the change in the soil moisture in the roadbed, particularly when the moisture content of the roadbed soil is very low.

4.2. Correlation Analysis between Deformation of Roadbed Soil and the Internal Directly Influencing Factors. The above correlation analysis shows that the air temperature variation significantly affects the change in the roadbed soil temperature and that the influence of rainfall on the roadbed soil
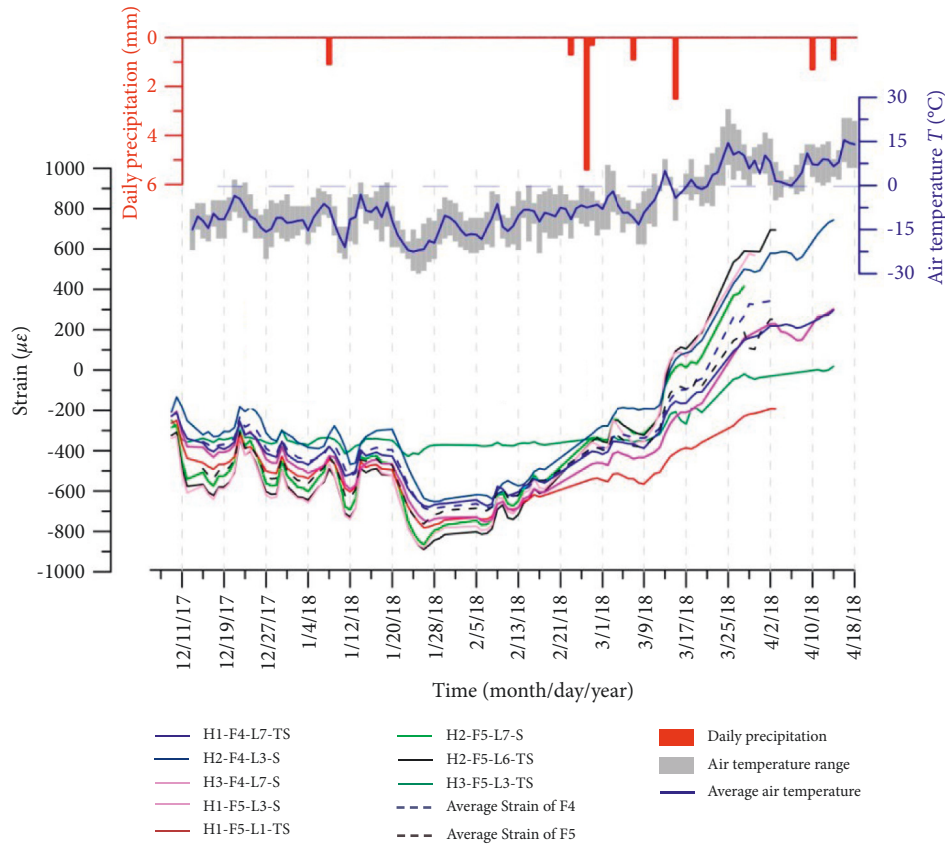
Figure 12: Curves of monitoring strain variation and calculated average strain in the F4 and F5 layers of the roadbed under climatic conditions.
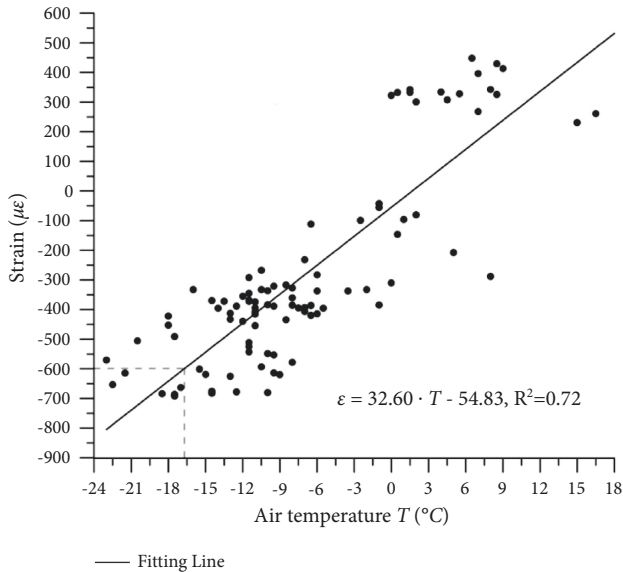

$$\varepsilon = 32.60 \cdot T - 54.83, \ R^2 = 0.72$$

Figure 13: Relationship between the average strain of the F4 layer soil of the roadbed and the air temperature.

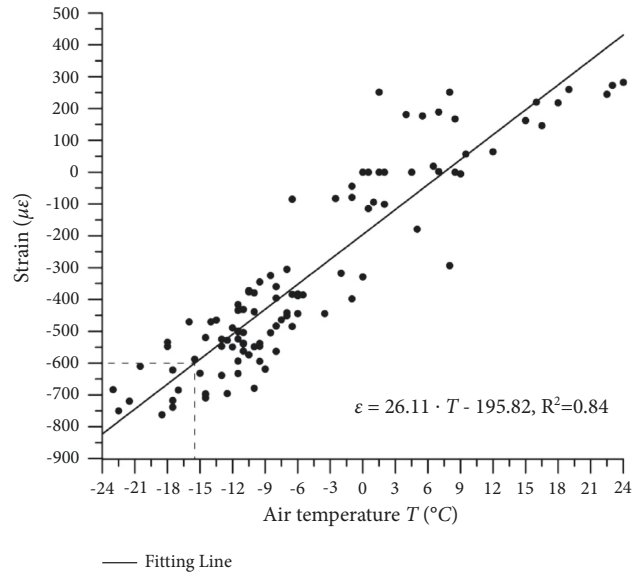$$\varepsilon = 26.11 \cdot T - 195.82, \ R^2 = 0.84$$

Figure 14: Relationship between the average strain of the F5 layer soil of the roadbed and the air temperature.

moisture is negligible. The correlation analysis between the roadbed soil deformation and the internal directly influencing factors (soil temperature and soil moisture) is presented below.

(1) Correlation Analysis between Soil Temperature and Soil Moisture of Roadbed. Table 5 shows the correlation analysis results of the soil moisture in the F5 and F3 layers of the roadbed in Figure 5 and the soil temperature in the F5 and
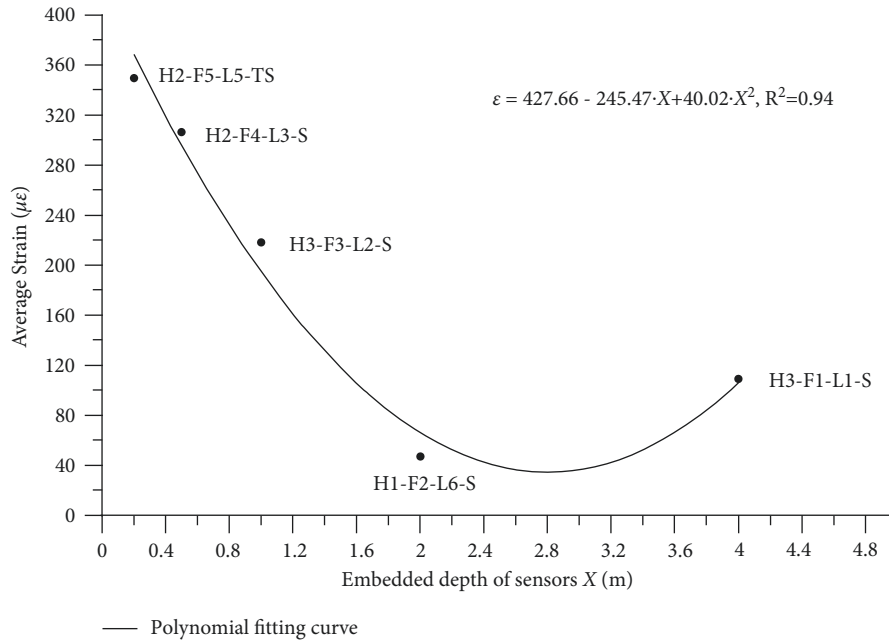
FIGURE 15: Relationship between the embedded depth of the sensors and the average strain of the soil.

F4 layers of the roadbed in Figure 6. From the F3 to F5 layers of the roadbed, the correlation coefficient between the change in the soil moisture and the change in the soil temperature is mostly less than 0.4, indicating that the change in the soil moisture is weakly correlated to the change in the soil temperature. When the soil moisture content in the upper part of the roadbed in the cold and arid areas is low, the change in the soil temperature of the roadbed has a weak effect on the moisture content.

(2) Correlation Analysis between Soil Deformation and Soil Moisture of Roadbed. Table 6 shows the correlation analysis results of the soil moisture recorded by the two moisture sensors placed in the F5 layer of roadbed cross sections 1 and 2 and the soil strain variation recorded by the two strain sensors placed beside the moisture sensor. From Table 6, it can be found that the correlation coefficients between the strain variation at different positions of the soil in the F5 layer and the moisture variation of the soil at the close position are mostly lower than 0.2, which is irrelevant. Therefore, it can be considered that the strain variation of the roadbed soil is independent of the change in the soil moisture.

(3) Correlation Analysis between Soil Deformation and Soil Temperature of Roadbed. Table 7 shows the correlation analysis results between the soil temperature variation in the roadbed recorded by the temperature sensors in the F5 and F4 layers and the soil strain variation recorded by the strain sensors at different locations in the same layer. Table 7 shows that the correlation coefficients between the soil temperature variation in the F5 and F4 layers of the roadbed and the soil strain variation at different positions in the same layer are greater than 0.8, representing a very strong correlation. Therefore, it is determined that the temperature change in

the roadbed soil is the key factor leading to deformation and cracking of the roadbed soil.

Combining the results listed in Tables 4 and 5, the soil strain change of the roadbed is found to be independent of the change in the soil moisture and is strongly correlated with the soil temperature variation, proving that the roadbed soil temperature and the soil moisture are weakly correlated indirectly. The results listed in Table 5 show that the two factors, soil temperature variation and soil moisture variation, that affect the deformation of the roadbed soil are independent of each other and that the soil strain is mainly affected by the soil temperature. The air temperature variation (external factor) is converted into soil temperature changes via soil heat conduction, and soil temperature changes (inner factor) are the direct factors leading to soil strain changes.

The above research reflects that the soil deformation of the test roadbed during the monitoring period is the temperature deformation.

4.3. Temporal and Spatial Variation Laws of Temperature Deformation of Roadbed Soil. The average strains in the F5 and F4 layers of the roadbed can be calculated from the strain monitoring data of the five sensors located in the F5 layer and the three sensors located in the F4 layer (Figure 12).

From the relationship between the average strain of the F5 and F4 layers and the air temperature in Figure 12, two statistical graphs of the average strain in the F4 and F5 layers as a function of the air temperature are drawn, and the data trend is linearly fitted, as shown in Figures 13 and 14.

Figures 13 and 14 show that the strain of the soil at different positions at the same level (same depth) inside the roadbed is different under the same air temperature, but the

average strain of the soil is linearly correlated with the air temperature overall. When the air temperature drops from 0°C to −24°C, the strain of the soil shows a negative value and a linear downward trend, indicating that the roadbed soil continues to shrink and deform as the air temperature drops. When the air temperature rises from 0°C to 18 or 24°C, the negative strain of the soil decreases, and the positive strain gradually increases, indicating that the shrinkage and deformation of the roadbed soil continue to decrease and turn into expansion and deformation during the rise in the air temperature. The fitting equations for the relationship between the average strain in the F4 and F5 layers of the roadbed and the air temperature variation are $\varepsilon_4 = 32.60 \cdot T$-54.83 ($R^2 = 0.72$) and $\varepsilon_5 = 26.11 \cdot T$-195.82 ($R^2 = 0.84$), respectively. The air temperatures corresponding to the critical tensile strain of 600 $\mu\varepsilon$ of the soil in the F4 and F5 layers of the roadbed are −16.72°C and −15.47°C, respectively. The slope of the fitted straight-line equation is the rate of change in the soil strain with the soil temperature, that is, the thermal expansion coefficient of the modified soil obtained from the field test. The thermal expansion coefficients of the F4 and F5 roadbed layers are 32.6×10^{-6} and 26.11×10^{-6}/°C, respectively, which differ from the linear expansion coefficients of the aeolian sand-modified soil measured in the laboratory [22], perhaps due to different sizes and boundaries. The tested expansion coefficient is the linear expansion coefficient of the sample strip along the long axis, and the size of the sample strip used for measuring the indoor thermal expansion coefficient was only 10 mm × 10 mm × 50 mm. However, the boundary of the surrounding soil affects the deformation of the modified soil in a large-scale field roadbed test, which can better reflect the actual scenario.

The embedded depth of the sensor is the distance below the datum level of the roadbed's upper surface. For example, the buried depth of the sensor in the F5 layer is 0.2 m from the roadbed's upper surface; hence, its hidden depth is 0.2 m, as are the buried depths of the four other layer sensors (Figure 4(b)). The relationship between the embedded depth of the sensors and the average strain of the soil can be obtained by calculating the absolute value of the average strain of the soil at different layers, as shown in Figure 15.

Figure 15 shows that the soil deformation of the roadbed does not decrease monotonously with the increase in the embedded depth of the sensor, but first decreases and then increases sensor. The polynomial fitting equation for the relationship between the average strain of the roadbed soil (ε) and the embedded depth of the sensor (X) is $\varepsilon = 427.66 - 245.47 \cdot X + 40.02 \cdot X^2$ ($R^2 = 0.94$), which indicates that the strain of the roadbed soil at different depths is different. The closer it is to the top surface of the roadbed, the greater the temperature deformation of the roadbed soil. Based on field monitoring data, aeolian sand-modified soil roadbed was found to shrink at low temperatures, and the shrinkage strain of the soil at different depths varied significantly at low temperatures. The strain on the surface of the roadbed exceeded the critical value of roadbed cracking strain; however, the strain near the bottom of the roadbed was lower than the critical value. The surface of the aeolian
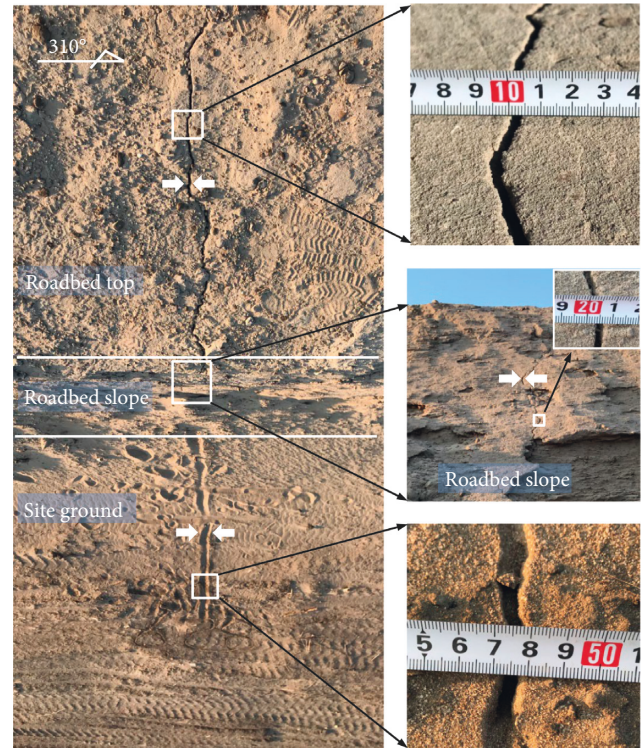

Figure 16: Top view and crack detail of the roadbed and site.

sand-modified soil road roadbed fractured in cold areas due to the process of low-temperature shrinkage and uneven surface and inner shrinking. Notably, the average strain at the bottom of the roadbed is greater than that of the soil above it, which may be attributed to the thermal expansion and contraction of the site at the bottom of the roadbed. Because the test section of the roadbed was built on a nonrigid site, although it was cleaned and rolled before paving the test section, the nonrigid site would still deform in cold climates, affecting the deformation of the test section's bottom. Field investigations in winter (December 27, 2017) revealed that the ground around the site where the test roadbed was located had ground cracks that were nearly perpendicular to the roadbed direction, and the ground cracks penetrated the roadbed Figure 16; the freeze-shrinkage deformation of the site where the test roadbed was located had a nonnegligible effect on the soil strain at the bottom of the roadbed.

5. Conclusions

Based on cracks induced in an aeolian sand-modified soil roadbed, this study considered a high-speed railway roadbed project under construction in a cold area to establish a large-scale in situ aeolian sand-modified soil roadbed to study the temporal and spatial variations in the temperature and deformation inside the roadbed of the aeolian sand-modified soil. The variations in the soil temperature, moisture, and strain of the roadbed under the influence of the climatic condition in this cold region were monitored using fiber Bragg grating (FBG) strain sensors embedded into the

roadbed. The correlation analysis method was used to analyze the correlation between the monitoring data (soil temperature, moisture, and strain) and the climatic conditions (air temperature and rainfall), to explore the correlation between the internal and external factors that cause the roadbed soil to deform, and to determine the main influencing factors that cause the roadbed soil to deform and crack. The following conclusions can be drawn from the study:

(1) The change in the soil moisture in the aeolian sand-modified soil roadbed had little effect on the deformation of the modified soil roadbed, and the strain variation in the roadbed soil was independent of the change in the soil moisture. The soil moisture content in the aeolian sand-modified soil roadbed was relatively low, and the very little rainfall in the cold and arid areas had a weak effect on the change in the soil moisture content in the roadbed.

(2) The direct cause of roadbed soil deformation in a low-air-temperature environment was found to be the variation in the roadbed soil temperature, and the variation in the roadbed soil temperature was due to the change in the air temperature. The roadbed boundary controlled the uneven spatial distribution of the soil temperature inside the roadbed, leading to significant differences in the thermally induced soil temperature. The surface of the aeolian sand-modified soil roadbed fractured in cold areas due to the process of low-temperature shrinkage and uneven surface and inner shrinking. The variation in the internal deformation of the modified soil roadbed had a strong correlation with the temperature change of the roadbed soil. The response of the roadbed soil temperature to the air temperature exhibited a hysteresis effect. The farther away from the roadbed surface, the more evident the hysteresis effect.

(3) The deformation of the aeolian sand-modified soil roadbed was linearly related to the air temperature change. A negative air temperature caused the roadbed soil to shrink and deform. The amount of soil shrinkage and deformation increased with the decrease in the negative air temperature. The air temperature changed from negative to positive, and the negative strain of the soil gradually decreased and turned positive. The deformation amount of the roadbed soil first decreased and then increased with increasing embedded depth of the sensor. The temperature deformation of the site foundation had a significant effect on the soil at the bottom of the roadbed.

In a field test with the aeolian sand-modified soil roadbed, the soil temperature field and soil strain field of the roadbed under the influence of the air temperature were intuitively monitored using a temperature-compensated optical fiber sensor. Some valuable data were obtained, and some laws based on the field test data were determined.

However, there remain shortcomings in the test; for example, the number of sensors was insufficient, and the soil deformation was measured only in one direction. In the future, increasing the number of monitoring points and performing the deformation monitoring of the roadbed soil in three orthogonal directions can help obtain a more in-depth and comprehensive understanding of the temperature deformation of the roadbed soil.

Data Availability

The field test data used to support the findings of this study are available from the corresponding author upon request.

Conflicts of Interest

The authors declare that they have no conflicts of interest regarding the publication of this article.

Acknowledgments

References

[1] G. J. Zhang, *Eremology*, China Forestry Press, Beijing, China, 1996.

[2] I. H. Kahn, "Soil studies for highway construction in arid zones," *Engineering Geology*, vol. 19, no. 1, pp. 47–62, 1982.

[3] A. Ghrieb, R. Mitiche-Kettab, and A. Bali, "Stabilization and utilization of dune sand in road engineering," *Arabian Journal for Science and Engineering*, vol. 39, no. 3, pp. 1517–1529, 2014.

[4] K. Moosavi and B. Kalantari, "Improving load bearing capacity of wind-blown sand using ordinary Portland cement," *Journal of Engineering and Computer Sciences(Oassim University)*, vol. 16, pp. 1267–1274, 2011.

[5] J. Wei, *Characteristic Research on Strength of Cement Improved Aeolian Sand and Deformation of Aeolian Sand Used to Fill Roadbed for Heavy Haul Railway*, Lanzhou Jiaotong University, China, 2017.

[6] M. López-Querol and S. Lopez-Querol, "Aeolian sands: characterization, options of improvement and possible employment in construction - the State-of-the-art," *Construction and Building Materials*, vol. 73, no. 30, pp. 728–739, 2014.

[7] Z. A. Rahman and M. A. Rahman, "The potential of cement kiln dust for the stabilization of dune sand in highway construction," *Building and Environment*, vol. 25, no. 4, pp. 285–289, 1990.

[8] M. Y. Al-Aghbari, Y. E.-A. Mohamedzein, and R. Taha, "Stabilisation of desert sands using cement and cement dust," *Proceedings of the Institution of Civil Engineers - Ground Improvement*, vol. 162, no. 3, pp. 145–151, 2009.

[9] S. Lopez-Querol, J. Arias-Trujillo, M. GM-Elipe, A. Matias-Sanchez, and B. Cantero, "Improvement of the bearing capacity of confined and unconfined cement-stabilized aeolian

sand," *Construction and Building Materials*, vol. 153, pp. 374–384. in press, 2017.

[10] G. F. Li, X. D. Shen, J. C. Wu, W. Dong, H. J. Xue, and X. Liu, "Experimental study on shrinkage deformation of aeolian sand concrete," *Bulletin of the Chinese Ceramic Society*, vol. 35, no. 4, pp. 1213–1218, 2016.

[11] S. A. Aiban, "A study of sand stabilization in Eastern Saudi Arabia," *Engineering Geology*, vol. 38, no. 1-2, pp. 65–79, 1994.

[12] H. I. Wahhab and I. M. Asi, "Improvement of marl and dune sand for highway construction in arid areas," *Building and Environment*, vol. 32, no. 3, pp. 271–279, 1997.

[13] G. S. Guo, Y. Zhang, and S. M. Du, "Grassroots-level shear strength experimental study of aeolian sand with cement," *Science Technology and Engineering*, vol. 15, pp. 327–331, 2017.

[14] B. X. Fu, *Research on Road Performance of Aeolian Sand with Different Mud Content*, Chang'an University, China, 2006.

[15] Y. K. Luo, Y. Q. Yuan, J. Wang, Y. D. Fan, and M. S. Feng, "Cure for wind-blown soil of rich water by cement stabilization," *Road Machinery & Construction Hechanization*, vol. 28, no. 01, pp. 29–32, 2011.

[16] F. B. Zhou, *Mechanism of and Solution for Frost Damage of Aeolian Sand Roadbed in Cold Region*, China University of Geosciences, Beijing, China, 2018.

[17] B. Bai, Q. K. Nie, Y. K. Zhang, X. L. Wang, and W. Hu, "Cotransport of heavy metals and SiO2 particles at different temperatures by seepage," *Journal of Hydrology*, vol. 597, Article ID 125771, 2021.

[18] B. Bai, R. Zhou, G. Q. Cai, W. Hu, and G. C. Yang, "Coupled thermo-hydro-mechanical mechanism in view of the soil particle rearrangement of granular thermodynamics," *Computers and Geotechnics*, vol. 137, no. 8, 2021.

[19] D. C. Li, "Study on road performance of cement stabilized aeolian sand," *Technology of Highway and Transport*, vol. 1, pp. 24–27, 2005.

[20] C. H. Wang, X. C. Wang, and X. Q. Tan, "Preparation of road aeolian sand curing agent and its mixture performance," *J Cent South Univ*, vol. 42, no. 1, pp. 192–198, 2011.

[21] Z. D. Su, J. Z. Sun, F. B. Zhou, and Y. Zheng, "Test and analysis of thermophysical properties of aeolian sand modified soil," *Water Resources and Hydropower Engineering*, vol. 50, no. 7, pp. 153–159, 2019.

[22] F. B. Zhou, Z. D. Su, M. N. Tian, G. Li, X. Chen, and J. Z. Sun, "Effect of clayey soil and fiber on thermal expansion of aeolian sand modified soil," *Bulletin of the Chinese Ceramic Society*, vol. 39, no. 01, pp. 199–205, 2020.

[23] G. Han, L. You, and Y. Q. Cheng, "Characteristics of ground wind regimes in the horqin sandy land when A cold front passed in spring," *Journal of Desert Research*, vol. 36, no. 4, pp. 1087–1096, 2016.

[24] L. W. Jing, Z. K. Wang, Z. Q. Meng, and B. Y. Li, "Discussion on the causes and recovery of desertification in horqin grassland," *Journal of lnner Mongolia University for Nationalities*, vol. 11, no. 3, pp. 105-106, 2015.

[25] *Inner Mongolia Communications Investment Co. LTD. [OL]*, http://www.nmgjttz.com/c/nmgjttzjt/2336.

[26] Q. L. Bao, X. L. Li, H. Y. Dai et al., "Climatic characteristics of cold and warm sharp turnaround in khorchin sandy land under global warming," *Journal of Northwest Forestry University*, vol. 35, no. 3, pp. 17–22, 2020.

[27] X. M. Liu, H. L. Zhao, and A. F. Zhao, *Wind-Sandy environment and Vegetation in the Horoin Sandy Land*, Science Press, China. Beijing, 1996.

[28] D. F. Li, T. X. Liu, X. Y. Liu, and L. M. Duan, "Analysis of soil temperature and freeze-thaw process in the horqin sandy land with sand-meadow land features," *Yellow River*, vol. 34, no. 5, pp. 82–85, 2012.

[29] P. Zhang, H. S. Zhang, and J. L. Du, "Analysis of the surface temperature over keerqin sand area in inner Mongolia," *Acta Scientiarum Nauralium Universitaties Pekinensis*, vol. 47, no. 4, pp. 655–663, 2011.

[30] C. T. Yue, X. Y. Liu, T. X. Liu, Y. Q. Fu, W. M. Cao, and Q. L. Liu, "Change rules of soil temperature and maximum freezing depth during freezing-thawing period in horqin sand and meadow," *Bulletin of Soil and Water Conservation*, vol. 36, no. 6, pp. 84–91, 2016.

[31] *TB 10202-2002, "Code for Construction on Roadbed of Railway*, China Railway Press, Beijing, 2002.

[32] R. You, L. Ren, and G. Song, "A novel fiber Bragg grating (FBG) soil strain sensor," *Measurement*, vol. 139, no. 6, pp. 85–91, 2019.

[33] J. B. Cai, *Study on Deformation Mechanism and Measures against Embankment's Longitudinal Cracking*, 2018.

[34] S. Q. Zhang, J. N. Lu, Z. Jiang, and L. Zhang, "Study of the correlation coefficients in mathematical statistics," *Mathematics in Practice and Theory*, vol. 39, no. 19, pp. 102–107, 2009.

[35] Y. X. Chen, "Understanding of the meaning of correlation coefficient," *Chinese Examination*, vol. 7, pp. 15–19, 2011.

[36] Y. Xiao, Y. Zhao, Z. D. Tu, B. Qian, and R. M. Chang, "Topology checking method for low voltage distribution network based on improved Pearson correlation coefficient," *Power System Protection and Control*, vol. 47, no. 11, pp. 37–43, 2019.

[37] F. Shao, C. Chen, M. J. Ge, Y. L. Hang, and W. H. Chen, "Analysis of technology innovation and application based on the power line loss Pearson algorithm," *Scientific and Technological Innovation*, vol. 14, pp. 54-55, 2017.

[38] R. A. Fisher, *Statistical Methods for Research Workers*, Hafner, New York, 13th edition, 1958.

[39] C. B. Zhu, G. Weatherill, F. Cotton, M. Pilz, DY. Kwak, and H. Kawase, "An open-source site database of strong-motion stations in Japan: K-NET and KiK-net (v1.0.0)," *Earthquake Spectra*, vol. 37, no. 3, pp. 2126–2149, 2021.

[40] K. W. Bozorgnia and Y. Bozorgnia, "Ground motion models for the horizontal components of arias intensity (AI) and cumulative absolute velocity (CAV) using the NGA-West2 database," *Earthquake Spectra*, vol. 35, no. 3, pp. 1289–1310, 2019.